Smart Agricultural Technology 11 (2025) 100990

Contents lists available at ScienceDirect

Smart Agricultural Technology

journal homepage: www.journals.elsevier.com/smart-agricultural-technology

Development of a stereo vision-based UGV guidance system for bareroot forest nurseries

Sharif Shabani [a], Ashish R. Mulaka [b], Thomas A. Stokes [d], Tanzeel U. Rehman [a], Yin Bao [b,c,*]

[a] Department of Biosystems Engineering, Auburn University, Auburn, AL, USA
[b] Department of Plant and Soil Sciences, University of Delaware, Newark, DE, USA
[c] Department of Mechanical Engineering, University of Delaware, Newark, DE, USA
[d] Weyerhaeuser Company, Aiken, SC, USA

ARTICLE INFO

Keywords:
Automatic guidance
Forest nursery inventory
Image processing
Stereo vision
Unmanned ground vehicle

ABSTRACT

The US forest nursery industry still relies heavily on manual labor for inventories during the growing season. Automating these processes could significantly reduce labor requirements while enhancing efficiency in counting and quality assessment of bareroot forest tree seedlings. In this study, we developed a stereo vision-based automatic guidance system for an unmanned ground vehicle (UGV) designed to follow forest nursery beds. The system was first developed and validated in simulation using the Webots simulator integrated with the Robot Operating System (ROS). A depth image processing algorithm based on the Hough transform was employed to detect bed edge-lines, with the image-derived relative bed angle serving as the error signal for a proportional controller that corrected the vehicle's heading and lateral deviation relative to the bed. The physical system was subsequently tested on a skid-steering UGV at a commercial forest nursery across four curved pine seedling beds with varying radii and lengths under an overcast condition, at ground speeds of 0.5 m/s and 1.0 m/s. The proposed vision guidance system successfully completed all eight trials without collisions with seedlings, traversing a total distance of 1422 m while achieving an average root mean square deviation of 0.05 m. These results underscore the potential of stereo vision-based guidance for automating nursery operations, paving the way for more efficient and reliable inventory and quality assessment in the forest nursery industry. Future research should validate and improve the system performance across a variety of bed geometries, soil characteristics, pine seedling heights, lighting conditions, and speeds.

1. Introduction

The U.S. forest nursery industry plays a vital role in supporting reforestation efforts, ensuring a sustainable supply of tree seedlings for forestry, ecosystem restoration, and conservation initiatives. More than 1.4 billion seedlings were produced in 2022 in the United States, with approximately 70 percent being bareroot seedlings [12]. Forest seedling production could be further driven by the increasing need for carbon sequestration as a strategy for climate change mitigation [5]. One of the most important tasks in forest nursery production is inventory, i.e., collection, organization, and analysis of data about the stock and quality of seedlings. The common practice for forest nursery inventory relies heavily on a manual sampling, where seedling counts and measurements from a limited number of short, linear plots within each seedling bed are used to estimate the total stock. Additionally, high seedling densities, typically ranging from 262 to 328 seedlings per linear bed meter, further complicate this task. This dependance on manual measurements makes the inventory process labor-intensive, time-consuming, and costly. Moreover, the ergonomic challenges faced by field workers during the inventory process can lead to discomfort and compromised data accuracy. The combination of computer vision and machine learning offers a promising solution to automate seedling counting with improved accuracy and efficiency. Recently, we developed an imaging system with a pushing mechanism to expose seedling stems and designed a long short-term memory model with convolutional neural networks (CNNs) to predict seedling count from optical flow [2]. The imaging system was carried by a manually driven tractor, which can be replaced by a low-cost and compact unmanned ground vehicle (UGV) to realize autonomous operation with reduced equipment and operational costs. Although commercial UGVs can be adapted to straddle a forest nursery

* Corresponding author at: Department of Plant and Soil Sciences, Department of Mechanical Engineering, University of Delaware, Newark, DE, USA.
E-mail address: yinbao@udel.edu (Y. Bao).

https://doi.org/10.1016/j.atech.2025.100990
Received 25 March 2025; Received in revised form 30 April 2025; Accepted 5 May 2025
Available online 6 May 2025

bed, to the best of our knowledge, an automatic guidance system has not been reported for the traversal of forest nursery beds.

Because forest nursery beds share similarities to the semi-structured environments of agricultural fields, existing works in automatic guidance systems for agricultural vehicles can be leveraged. Global navigation satellite system (GNSS) sensors are commonly used for the automatic guidance of agricultural vehicles. However, real-time kinematic (RTK) correction coupled with dual GNSS antenna and inertial navigation sensors is typically needed to achieve accurate localization and heading estimation for crop row following, especially for vehicles that can perform zero-radius turns [14]. Color cameras offer a low-cost vision-based navigation sensor to detect crop rows and estimate the relative lateral offset and orientation of a vehicle. Crop rows are typically detected in near-infrared or red-green-blue (RGB) images using threshold-based image segmentation algorithms [1] or deep learning-based semantic segmentation models [4,13]. Subsequently, the segmented crop rows can be modeled as either lines or curves through image processing algorithms such as Hough line transform [1] and adaptive multi-ROI [13]. Depth sensors measuring the three-dimensional (3D) environment offer another approach for crop row navigation with simplified crop segmentation from the ground due to elevation difference. Passive stereo cameras have been used to find the center point of a track between crop rows in the elevation map for auto-guidance of a tractor [7]. Active Time-of-Flight (ToF) cameras were used for under-canopy navigation [6]. Light detection and ranging (LiDAR) sensors have been used to detect crop row orientation and lateral position by analyzing the histogram of the point cloud projection onto the ground plane [11]. Among the reviewed navigation sensors, all are applicable for forest nursery bed following except for ToF cameras, which may not operate reliably under direct sunlight. Considering cost, RTK-GNSS sensors can be prohibitively expensive for forest nurseries, and signal loss poses a risk of crop damage. LiDAR sensors can function under outdoor lighting conditions; however, their spatial resolution is generally low, making them more suitable for detecting large structures such as orchard trees. While LiDAR sensors are generally less expensive than RTK-GNSS systems, they remain relatively costly. RGB cameras offer a cost-effective solution with high spatial resolution but rely on robust crop segmentation methods, which can be sensitive to color variations caused by crop growth and stress, necessitating parameter adjustments or additional data curation and model training. Finally, stereo cameras reconstruct depth images by performing dense stereo matching of image pairs, offering high spatial resolution capable of capturing both the structure of raised beds relative to tractor tracks and the growth of seedlings over time. In addition, stereo cameras are a cost-effective option. The specific research objective was to develop and evaluate a stereo vision-based automatic guidance method for a commercial UGV to follow forest nursery beds in simulation and at commercial nurseries.

The following sections are structured as follows: Section 2 describes the hardware and software design of the stereo vision-based UGV guidance system, including the development and validation of the depth image processing algorithm. Section 3 presents simulation and field-test results, analyzes the bed-following performance, compares outcomes with existing stereo vision guidance methods, and discusses current system limitations along with potential improvements. Lastly, Section 4 summarizes key findings and highlights implications for future research and practical application in forest nursery operations.

2. Materials and methods

2.1. Hardware design

A robotic platform was developed based on a skid-steering UGV with a three-point electric lift (Amiga, Farm-ng, CA, USA). The skid-steering mechanism steers by turning the wheels on one side of the vehicle at a different speed than on the other side. The UGV employs four brushless DC hub motors to achieve a compact, lightweight design at a relatively low cost. Since a standard forest nursery bed is 1.2 m wide with a 0.3 m wide tractor path on each side, the track width of the UGV was configured to 1.5 m. Given the 0.1 m wheel width, the lateral vehicle offset should be within ± 0.1 m to avoid contact with the nursery bed. A front-facing stereo camera with a horizontal and vertical field of view of $110^\circ \times 70^\circ$ (ZED 2i, Stereolabs, CA, USA) was mounted on the electric lift for robot heading estimation. The ZED software developer kit (SDK) was used to retrieve the RGB stereo image pairs and depth images with a resolution of 1920×1080 at 30 frames per second (FPS). The depth image was computed using the "performance" mode of the ZED SDK to enable the maximum frame rate. An RTK-GNSS receiver with a 10 Hz output rate (Reach RS2, Emlid, Budapest, Hungary) was installed on the UGV for robot localization and data georeferencing. Four downward-facing stereo cameras (OAK-D S2, Luxonis, Boulder, CO, USA) were mounted on the front tool bar for seedling imaging. A light-emitting-diode (LED) light bar was installed on the toolbar to illuminate the pine seedlings that were being pushed by a roller. An edge computer (Jetson AGX Orin, NVIDIA, CA, USA) was housed in an electrical enclosure to interface with a microcontroller (Feather M4 CAN Express, Adafruit, New York, NY, USA) that ran a custom CircuitPython script to handle the communication between the edge computer and the UGV. The UGV was controlled by two commands: linear velocity and angular velocity. All the cameras and the RTK-GNSS receiver were connected to the edge computer via a universal serial bus (USB). A 12 V 50Ah lead acid battery was used to power the sensing and control system, independent from the power system of the UGV. The external battery aimed to extend the operation time of the entire robotic platform. Fig. 1A shows the UGV straddling a bareroot seedling bed at a commercial forest nursery, highlighting the locations of three key components.

2.2. Software design

Webots [10] was used to simulate a forest nursery environment and the UGV. The UGV was modeled as a rectangular body that spanned 2.1 m in length, 1.8 m in width, and 1.5 m in height. Four wheels of 0.28 m radius were modeled with rubber as surface material. Each of the four wheels was equipped with a virtual electric motor. Virtual sensors including a *GPS*, a *Camera*, and a *RangeFinder* were added to the UGV model. A stereo camera was modeled using the Camera and the *RangeFinder* to provide RGB and depth images and placed at the front of the robot at 1.5 m above ground. Ten straight 20×1.2 m nursery beds with virtual seedlings were also modeled in SolidWorks (Dassault Systèmes, Waltham, MA, USA) and imported into Webots. Fig. 1B shows the UGV and the nursery beds in the Webots simulation.

Robot Operating System 2 (ROS2) [8] Foxy Fitzroy was used to develop a central control system that consisted of five ROS nodes for managing the sub-systems of the UGV (Fig. 2). The Vision-Based Heading Estimation Node estimates UGV heading angle with respect to the seedling bed. The Steering Guidance Node receives vehicle heading and location data and computes the steering rate to correct the heading error. The UGV Control Node receives steering commands and controls the speeds of the drive motors. The GPS Node receives location data and publishes them to other nodes. The Seedling Imaging Node records georeferenced stereo videos for seedling inventory.

Specifically, the Vision-Based Heading Estimation Node processes real-time depth images to detect the orientation of the seedling bed with respect to the UGV. The elevation differences between the raised seedling beds and the tracks were leveraged for the detection of bed edges in the depth images. The depth image processing pipeline was implemented using the OpenCV library [3]. The depth image was first downsampled to 640×360 to speed up subsequent processing. Then the downsampled depth image was smoothed using the OpenCV *GaussianBlur* function before applying Canny edge detection to highlight significant elevation changes. In simulation, we tested Gaussian kernel sizes 3×3, 5×5, 7×7, and 9×9 alongside hysteresis threshold pairs ranging

Fig. 1. A stereo vision-guided UGV for bareroot forest nursery inventory. (A) Physical UGV. (B) Webots simulation.

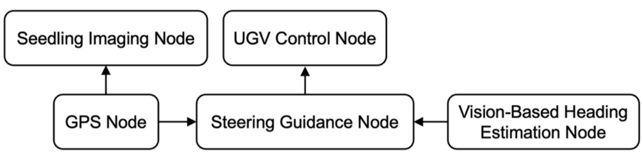

Fig. 2. ROS nodes and their communication.

from 0 to 100. A 5 × 5 kernel combined with thresholds of [20, 60] provided the best balance between accurately preserving true bed edges and suppressing noise from sporadic depth discontinuities. The resultant edge map was cropped using a predefined trapezoidal window to extract the region of interest (ROI) for the straddled seedling bed. Next, the *HoughLinesP* function [9] was used to detect line segments from the edge pixels within the ROI. The distance resolution, angle resolution, and threshold of the accumulator were set to 2 pixels, 180°, and 20, respectively. Additionally, the minimum line length and the maximum line gap were limited to 30 pixels and 5 pixels, respectively. Each detected line was then classified as either the left or right bed edge. In the image coordinate system with the X axis pointing right and the Y axis downward, lines representing the left bed edge have negative angles, while those for the right bed edge have positive angles. Specifically, a line with an angle between −65° and −45° was assigned to the left edge, and one with an angle between 45° and 65° was assigned to the right edge. An image-derived relative bed angle, δ, in radians was computed by summing the average angles of the two bed edges using Eq. (1)

$$\delta = \frac{\sum_{i=1}^{n} AL_i}{n} + \frac{\sum_{j=1}^{m} AR_j}{m} \tag{1}$$

where AL_i denotes the angle of the ith of the n total Hough lines belonging to the left edge of the bed, and AR_j denotes the angle of the j-th of the m total Hough lines belonging to the right edge of the bed. To mitigate the impact of momentary failure of bed edge-line detection and reduce the noise in the image-based bed angle and, a median filter was employed to smooth the five most recent measurements. Additionally, if no Hough lines were detected for either edge of the bed, the linear and angular velocities of the UGV were set to zeros. Fig. 3 shows a simulated scene and the intermediate image processing steps. A proportional

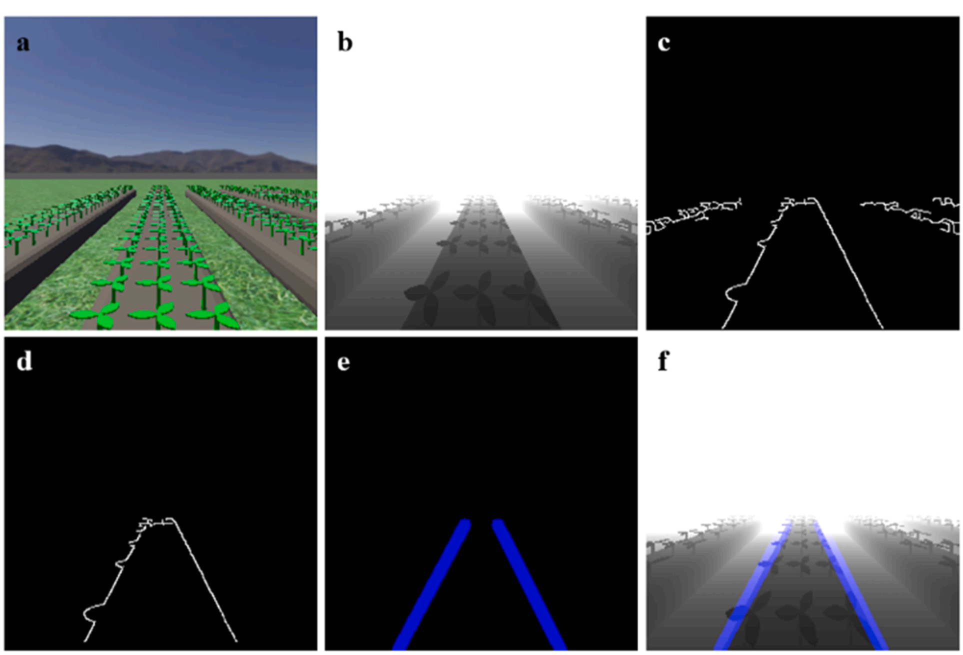

Fig. 3. An example scene and image processing steps for robot heading estimation. (a) RGB image showing the scene. (b) Depth image. (c) Edge detection. (d) Region of interest. (e) Hough line detection. (f) Bed edge detection overlaid on the depth image.

controller with a proportional gain K_p was employed to compute a target UGV angular velocity ω needed to align the vehicle heading with the bed orientation using Eq. (2). A gain-sweeping experiment was conducted in Webots to determine the optimal K_p from 0.1 to 1.0 with a step size of 0.1 using evaluation metrics described in the next section.

$$\omega = K_p \times \delta \tag{2}$$

2.3. Evaluation

The stereo vision-guided bed following algorithm was evaluated in the Webots simulation and at a commercial forest nursery at two ground speeds of 0.5 m/s and 1.0 m/s. The 0.5 m/s speed follows our previous study, where a machine vision system was developed to count pre-harvest pine seedlings pushed by a roller at that speed [2]. The 1.0 m/s speed was chosen as our desired ground speed for pine seedling counting after emergence. At this early stage, the small seedlings do not require a mechanical roller to separate them for imaging and thus a higher ground speed can be used. In the simulation environment, the desired path was configured as a lawnmower pattern. A waypoint following a navigation algorithm based on a heading error was implemented to complete headland turning when the bed was not detected. The root mean square deviation (RMSD) between the trajectory of the virtual UGV and the planned path was calculated to tune the parameters of the proposed algorithm in the simulation environment. Field tests were conducted at a commercial forest nursery located in South Carolina, USA (the specific location omitted for privacy reasons). The nursery produces bareroot loblolly pine seedlings on curved beds with varying lengths and radiuses due to the use of a center-pivot irrigation system. Four beds across a pie-shaped area (1/8 of the full circle) under the center pivot were selected for testing. The UGV was manually positioned at the beginning of each bed before testing. Then, the UGV automatically stopped if the bed was not detectable at the other end of the bed. The travel direction was alternated between consecutive beds, and the pattern was switched between the two ground speeds. RMSD, mean absolute deviation (MeAD), maximum absolute deviation (MaAD), and standard deviation of deviation (SDD) were calculated to assess the bed following performance for the field tests using Eqs. (3)–(7).

$$d_i = \sqrt{(x_i - \hat{x}_i)^2 + (y_i - \hat{y}_i)^2} \tag{3}$$

$$RMSD = \sqrt{\frac{\sum_{i=1}^{N} {d_i}^2}{N}} \tag{4}$$

$$MeAD = \frac{\sum_{i=1}^{N} |d_i|}{N} \tag{5}$$

$$MaAD = \max(|d_1|, |d_2|, \cdots, |d_n|) \tag{6}$$

$$SDD = \sqrt{\frac{\sum_{i=1}^{N} (d_i - \overline{d})^2}{N}} \tag{7}$$

where i denotes the index of a UGV position measurement, (x_i, y_i) denotes the UTM coordinates of the UGV, $(\hat{x}_i, \hat{y}_i)$ denotes the UTM coordinates of the nearest point to (x_i, y_i) on the planned path, d_i denotes the deviation between (x_i, y_i) and $(\hat{x}_i, \hat{y}_i)$, N denotes the total number of UGV position measurements, and $\overline{d}$ denotes the average deviation of UGV position measurements from the planned path. The planned paths for the physical nursery beds were obtained by manually driving the UGV along each bed and surveying the bed centerline at intervals of approximately 6.7 m. At each survey point, the UGV was manually positioned to place the onboard GNSS receiver above the center of the bed.

The surveyed longitude and latitude coordinates were converted to Universal Transverse Mercator (UTM) coordinates, followed by cubic interpolation to derive the desired path in the form of waypoints at 0.01 m intervals for each bed. The cubic interpolation was performed using Python 3.12.1 and the CubicSpline library from SciPy 1.11.4. The boundary condition was set to ‘natural,’ ensuring the second derivative at both endpoints is zero, and extrapolation was turned off to avoid out-of-bounds points based on the first and last intervals. For every recorded position along the UGV trajectory, the closest waypoint on the desired path was identified using a KDTree, and their Euclidean distance was calculated as the deviation of the UGV from the desired path. The sign of deviation was defined in two ways. First, in the UTM coordinate system, a positive deviation occurs when the UGV position is farther from the bed’s center of curvature than its nearest waypoint on the bed centerline, while a negative deviation occurs when the UGV position is closer to the center of curvature of the than its nearest waypoint. Second, in the UGV’s local coordinate system, a positive deviation was defined as the UGV being positioned to the left of the bed center, while a negative deviation was defined as it being positioned to the right.

At each UGV position, the vehicle’s heading angle was computed from GNSS data by fitting a second-degree polynomial to the measurements within a window of ±7 GNSS points and then calculating the polynomial’s derivative and arctangent at the UGV’s position. The same procedure was applied to determine the local bed orientation at the nearest waypoint on the bed centerline. The GNSS-derived relative vehicle heading angle was obtained by subtracting the bed orientation from the UGV’s heading angle, with its sign being opposite to that of the image-derived relative bed angle.

3. Results and discussion

3.1. Simulation result

A stereo vision-based guidance system was successfully developed for a commercial UGV to follow forest nursery beds. Forest nurseries are often located in remote areas, making frequent data collection and robot testing logistically challenging. The combination of Webots robotics simulation and ROS2 provides a powerful tool to accelerate the development of the depth image processing pipeline for vehicle heading estimation and closed-loop steering control without real imagery data collected from nurseries. The stereo vision-based guidance algorithm successfully controlled a virtual UGV to traverse all ten straight beds in the Webot simulation environment with an optimal proportional gain of 0.8. At a ground speed of 0.5 m/s, the algorithm achieved an RMSD of 0.011 m during bed following. As the ground speed was increased to 1 m/s, the RMSD for bed following increased to 0.030 m. The increased RMSD at the higher ground speed of 1 m/s was likely due to reduced reaction time for the guidance algorithm, leading to larger deviations as the UGV adjusted its trajectory to stay within the track boundaries. However, at both speeds, the simulated RMSD values were far below the threshold of 0.1 m which can cause collision with the bed. Fig. 4 shows the simulated robot trajectory at a ground speed of 0.5 m/s and the planned path. It can be observed that the virtual UGV oscillated around the planned path with relatively high tracking errors in the beginning section of the bed after a headland turn. However, the tracking error decreased over distance as the proportional controller minimized the tracking error to a steady state. The results confirmed the effectiveness of the stereo vision-based guidance algorithm in simulation.

3.2. Bed edge-line detection

The transition from simulation to real-world forest nursery environments was relatively smooth, requiring minor adjustments to the image processing algorithms. Some differences in the depth images between simulated and real-world nursery beds initially caused challenges for the guidance system to operate properly. The simulated beds presented clear edges in the depth image for bed edge-line detection, even

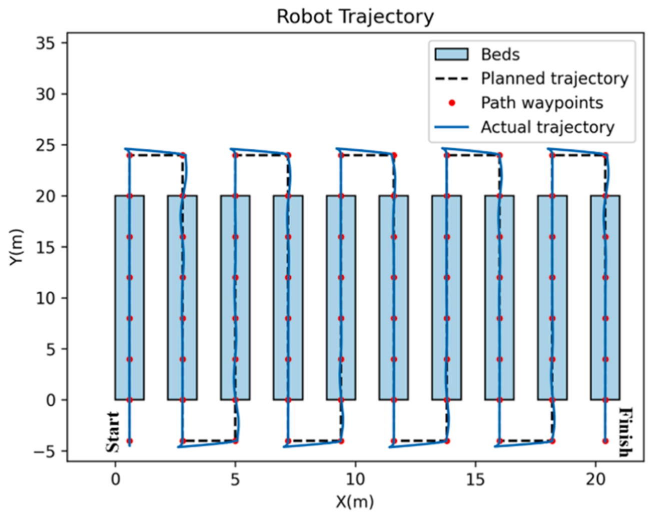

Fig. 4. Robot trajectory vs planned path in simulation at a ground speed of 0.5 m/s.

though the simulated seedlings introduced some noises. However, the height of the actual nursery beds relative to the tracks was not sufficient to present strong edges in the stereo camera-based depth images. Because bareroot forest seedling production prefers sandy soil, it was likely that the sandy soil near the edge of the beds was washed off to the tracks due to irrigation and rainfalls. Consequently, the edge detection algorithm resulted in far more noisy and less continuous segments at the two sides of the bed compared to the simulated environment. Moreover, some Hough lines were detected on and off within the bed due to the uneven spacing between seedling rows on the bed, introducing errors to the relative bed angle estimation. Therefore, additional filtering based on the slopes of the Hough lines was implemented at the time of field testing to exclude those detected lines within the bed. Fig. 5 shows qualitative results of bed edge-line detection in the depth image and their bed angles relative to the UGV heading in the image space. The depth images show invalid depth values at both left and right edges of the beds because occlusion occurs at depth discontinuities for the physical stereo camera and the correspondences cannot be matched for the stereo image pair. In addition, the occluded areas at the left sides of the beds tend to be more than those at the right sides due to the use of the left camera as the reference. Therefore, the Hough transform detected lines at the transition between a track and its connected occluded area and at the transition between the pine seedlings in the edge row and its connected occluded area. The algorithm-derived averaged edge-line can vary within or in close proximity to the occluded area depending on the linearity of the contour curves on the two sides of the occluded area. For instance, the detected left bed edge-line for Bed 2 at 0.5 m/s aligns with the track in Fig. 5-A2, while the detected left bed edge-line for Bed 1 at 1.0 m/s aligns with the seedlings in Fig. 5-B1.

3.3. Bed following performance

The physical UGV was successfully tested on real-world nursery beds, completing a total travel distance of 1422 m without collisions or human intervention. The lengths, radiuses, and number of survey points for the four test beds are detailed in Table 1. As the lengths and arc radii of Beds 1–4 increase, the number of survey points collected also increases. Table 2 shows detailed bed following metrics for each bed at the two ground speeds. The precision is rounded to the nearest 0.01 m to reflect the centimeter-level precision of RTK-GNSS positioning. Overall, the lateral deviation in terms of average RMSD and MeAD did not exceed 0.05 m, remaining well below the 0.1 m threshold. Additionally, the average SDD values at both speeds stay within 0.03 m. Therefore, at a 95% confidence level, the UGV's lateral deviations from the bed centerline are expected to be within ± 0.1 m. On the other hand, five out of the eight trials resulted in MaAD values over the 0.1 m threshold.

Fig. 6 illustrates the lateral deviations of the UGV trajectories from the centerlines of the four nursery beds. At the test speed of 0.5 m/s, a significant systematic deviation was observed, with the UGV tending to travel slightly to the right of the bed center. This was indicated by an overall negative deviation for Bed 1 and 3 when the UGV traveled southbound and an overall positive deviation for Bed 2 and 4 when the UGV traveled northbound. The likely cause was the position of the stereo camera: although mounted at the center of the robot, depth images were generated using the left camera of the stereo pair. This introduced a physical offset of 0.06 m due to the 0.12 m baseline of the stereo pair. In terms of RMSD, MeAD, and MaAD at a speed of 0.5 m/s (Table 2), their values for Bed 2 and 4 are more than twice as high as those for Bed 1 and 3. The significant systematic deviation also implies that the proportional controller operated as intended, without understeering or oversteering. At the speed of 1.0 m/s, the overall positive deviation for all four beds suggests that the UGV tended to stray farther from the pivot point of the center-pivot irrigation system. This behavior can be attributed to higher wheel slippage on sandy soil at increased speed and to the centrifugal force overpowering the proportional controller, leading to slight understeering.

Fig. 7 presents histograms illustrating the bed-following lateral

Table 1
Information about the four nursery beds for field testing.

Bed ID	Arc Length (m)	Arc Radius (m)	Number of survey points
1	83	124	14
2	116	168	18
3	197	284	30
4	315	444	44

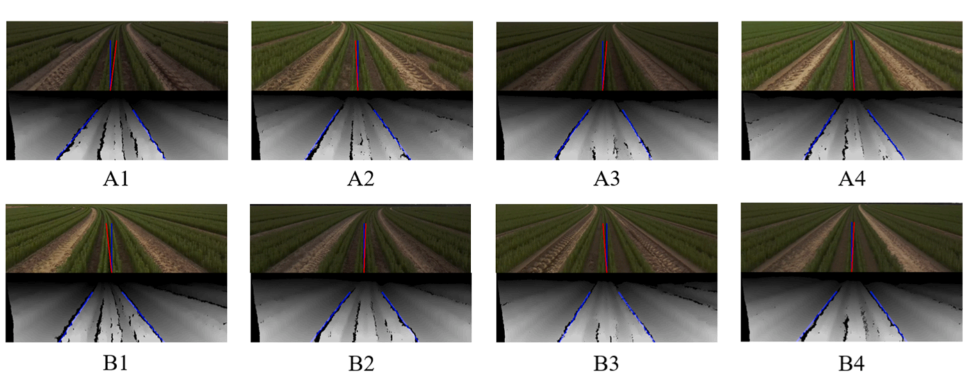

Fig. 5. Examples of bed edge-line detection results in the depth images (blue lines in the grayscale images) and the bed angles (red lines) relative to the vehicle heading (blue lines) in the RGB images for eight trials. Black pixels in the depth images indicate no depth values. A: 0.5 m/s. B: 1.0 m/s. 1–4: Bed ID.

Table 2
Bed following results.

Ground Speed (m/s)	Bed ID	Travel Direction	RMSD (m)	MeAD (m)	SDD (m)	MaAD (m)
0.5	1	South	0.03	0.02	0.02	0.03
	2	North	0.07	0.07	0.02	0.11
	3	South	0.03	0.03	0.02	0.03
	4	North	0.09	0.08	0.03	0.16
	Average	N/A	0.05	0.05	0.02	0.08
1	1	North	0.06	0.05	0.02	0.11
	2	South	0.05	0.04	0.03	0.11
	3	North	0.05	0.04	0.03	0.11
	4	South	0.04	0.04	0.02	0.09
	Average	N/A	0.05	0.04	0.03	0.11

deviations for the eight trials where "A" indicates the low speed, "B" the high speed, and the numeral corresponds to the bed ID. All the histograms tend to show normal distributions but with different means within ±0.1 m acceptable deviation limits from the bed centerline. Trials A1, A3, and B4 consistently remained within the ±0.1 m limits. Trials A2, B1, B2, and B3, however, showed occasional deviations exceeding the limits. Specifically, the MaADs for these four trials surpassed the implied 0.1 m limit, but only by approximately 0.01 m. This small excess is comparable to the precision of the RTK-GNSS unit in motion, suggesting the measured MaADs in these cases might slightly overestimate the actual vehicle deviation. Trial A4 exhibited frequent deviations beyond the acceptable limits. This high failure rate is likely due to a combination of the camera offset and the travel direction effects discussed previously. If a 0.06 m camera offset correction is applied to the low-speed deviation data, where the controller is assumed to be operated properly, the histograms for trials A2 and A4 would shift leftward by 0.06 m, and those for trials A1 and A3 would shift rightward by 0.06 m. This correction would result in lower calculated average RMSD, MeAD, and MaAD values compared to those initially measured. This specific correction is inappropriate for the high-speed trials, where the controller's understeering likely dominates deviation causes over the camera offset.

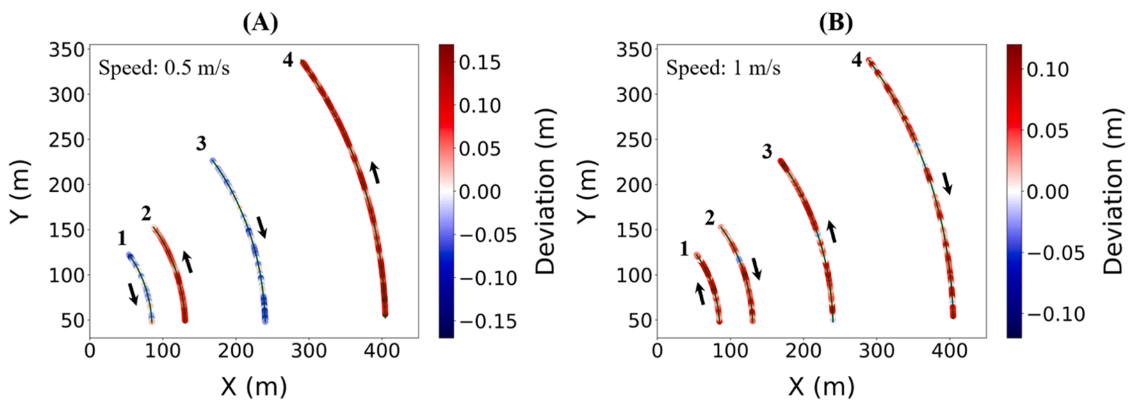

Fig. 6. Deviation of the UGV trajectory (colored dots) from the centerlines of the nursery beds at ground speeds of (A) 0.5 m/s and (B) 1.0 m/s. A positive deviation denotes that the UGV is positioned farther from the origin than its closest point along the bed centerline. The UTM coordinates were translated and slightly rotated to a local coordinate system for better visualization.

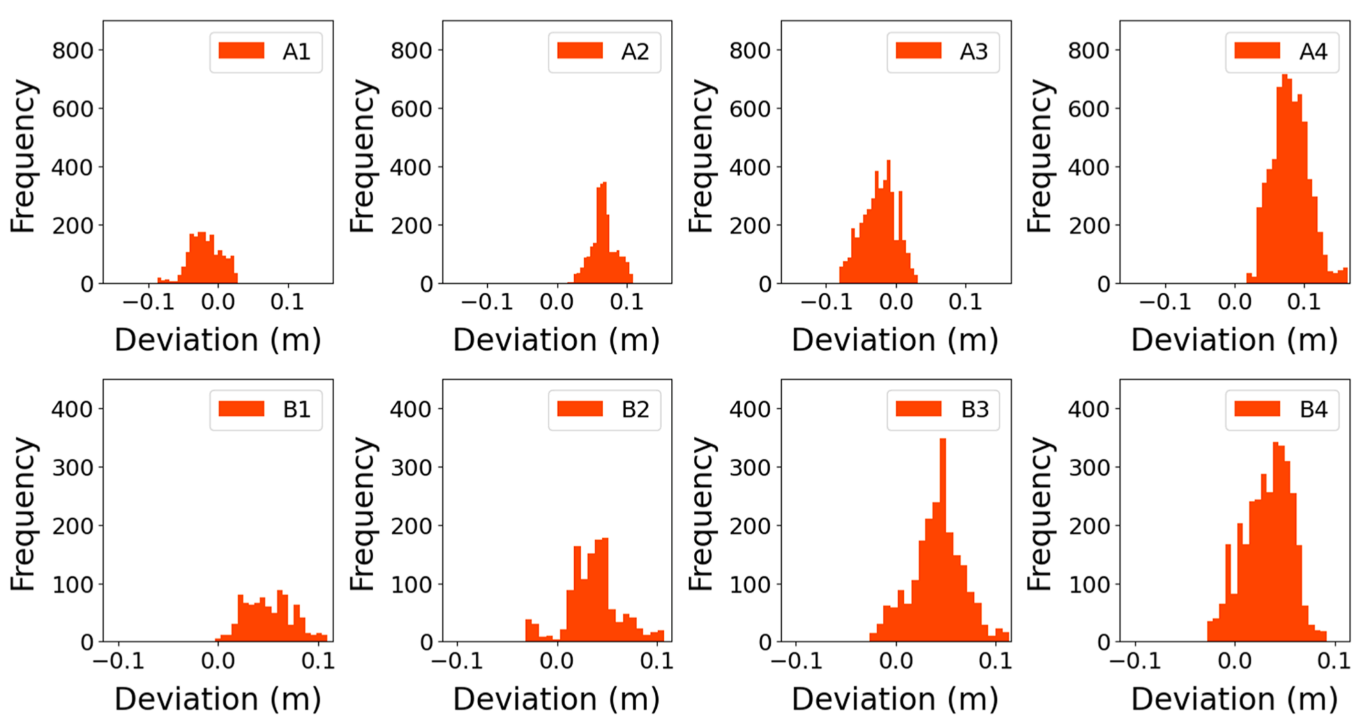

Fig. 7. Histograms of the bed-following deviations for eight trials. A: 0.5 m/s, B: 1.0 m/s, 1–4: Bed ID.

Consequently, at the high speed, assuming negligible camera offset, the measured average RMSD, MeAD, and MaAD should approximate the true vehicle tracking performance. It is important to consider that our manual path surveying may introduce its own errors. Our analysis suggests this survey error could be up to 0.06 m, potentially exceeding the uncertainty of the RTK-GNSS positioning itself. This level of survey error could contribute significantly to the large MaAD observed in trial A4. Since no collisions with any beds were observed during the field trials, we interpret the large MaAD measured for bed 4 primarily as a systematic error in the surveyed reference points for that bed, rather than solely poor vehicle tracking. Finally, it was observed that the sloped sides of the raised beds might have provided some passive steering assistance to the UGV when its wheels approached the bed edges.

Figs. 8 and 9 show the GNSS-derived relative vehicle angle, the image-derived relative bed angle, and the GNSS-derived relative vehicle deviation for the four beds at two ground speeds, respectively. The GNSS-derived relative vehicle angle oscillates around 0°, with its sign aligning with the direction of change in the corresponding GNSS-derived relative vehicle deviation. Specifically, the GNSS-derived relative vehicle deviation increases when the GNSS-derived relative vehicle angle is positive and decreases when the angle is negative. This is the result of the relative vehicle deviation being essentially the time integral of the relative vehicle heading. Unlike the smoother GNSS-derived relative vehicle angle, the image-derived relative bed angle has higher variability and does not oscillate around 0°. This increased variability likely results from errors in the depth image-based bed edge-line detection due to occlusion. Moreover, the sign of the oscillation point of the image-derived relative bed angle depends on the general steering direction. This is the result of the image-derived relative bed angle being based on the bed image in a long look-ahead window of approximately 20 m. When traveling southbound (Fig. 6: A1, A3, B2, B4), the UGV is generally expected to steer right to follow the right-curving bed (Fig. 5: A1, A3, B2, B4). Conversely, during northbound travel (Fig. 6: A2, A4, B1, B3), the UGV typically steers left to follow the left-curving bed (Fig. 5: A2, A4, B1, B3). The median image-derived relative bed angles for trials A1–A4 and B1–B4 are 0.66°, −0.37°, 1.43°, −0.37°, −0.04°, 3.25°, 1.09°, and 2.22°, respectively, with the signs aligning with the expected steering directions except for trial B3. The image-derived relative bed angle tends to counter the trends of the GNSS-derived relative vehicle angle rather than mirroring them, especially at the higher ground speed (Fig. 9). When it moves in the opposite direction of the GNSS-derived relative vehicle angle, this suggests that the proportional controller is actively aligning the UGV's heading with the bed orientation and reducing vehicle deviation from bed centerline.

Table 3 presents the percentage of frames in which simultaneous detection of both left and right bed edge-lines failed for each trial. At 0.5 m/s, the average failure rate across all beds was 6.14 %, rising to 11.60 % at 1.0 m/s. This increase likely reflects greater motion blur and depth-image noise at higher speed. Although Beds 1–4 exhibit progressively larger arc radii (Table 1), their failure rates do not follow a corresponding pattern. On average, detection success improves with increasing bed radius, consistent with the notion that tighter curvature hampers Hough-line fitting, but Bed 2 (which has the second highest curvature) shows the highest failure rate. This lack of direct correlation implies that, while speed is a dominant factor, bed curvature alone does not govern detection performance; bed-specific characteristics such as the uniformity and contrast of the edge elevation relative to the tractor tracks also play a critical role. Despite seemingly high percentages of detection failure, these instances were transient. The UGV's forward momentum bridged these brief gaps, giving the system time to reacquire the bed edges and preserve continuous, collision-free bed following.

3.4. Comparison with related studies

Compared to stereo vision-based tractor guidance studies with similar vehicle widths, test speeds and validation sensors (e.g., RTK-GNSS), our system achieved comparable [15] or worse [7] tracking performance (Table 4). Our lower tracking performance could stem from the skid-steering mechanism, which is not as smooth as the Ackermann steering of conventional tractors. Moreover, wheel slip was worsened by the sandy soil at the forest nursery. Such a challenge might not be present for cotton and soybean fields as in Zhang et al. [15] and Kise et al.

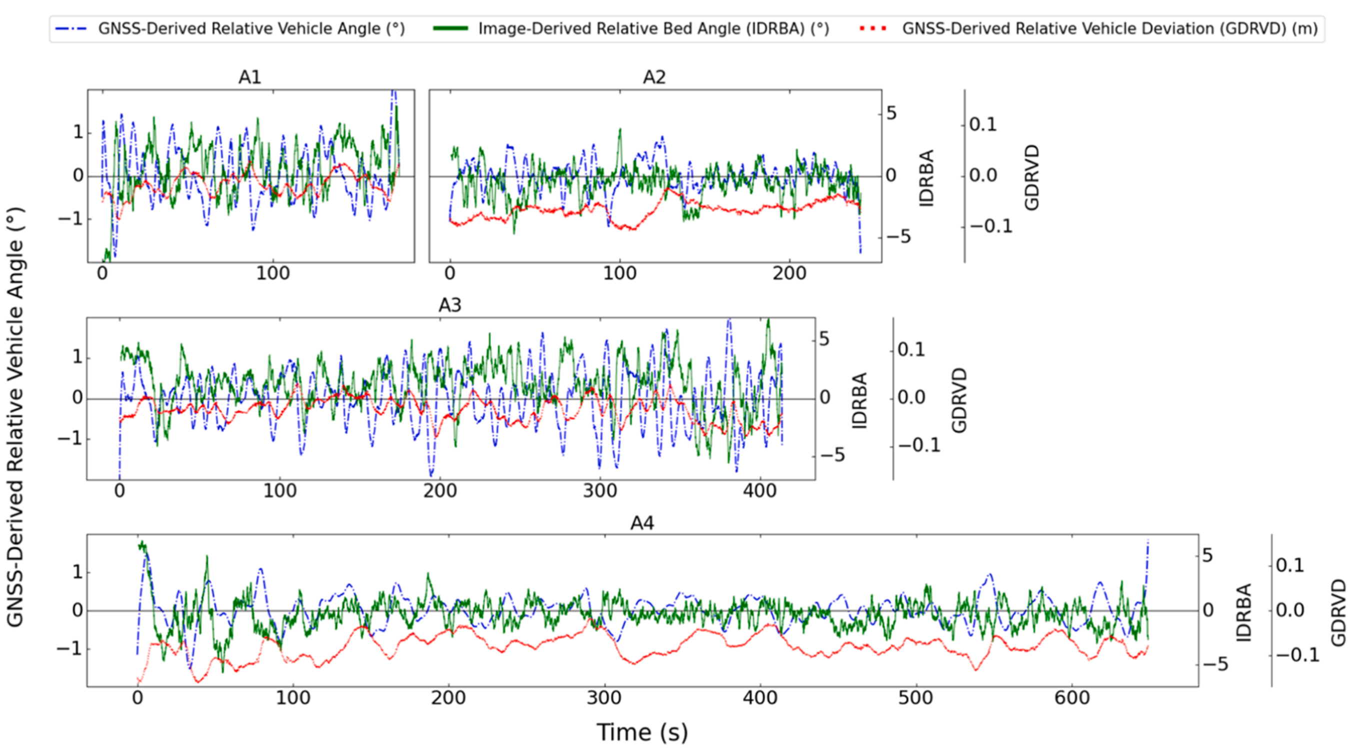

Fig. 8. GNSS-derived relative vehicle angle and deviation vs. image-derived relative bed angle at a ground speed of 0.5 m/s (A) for beds 1–4.

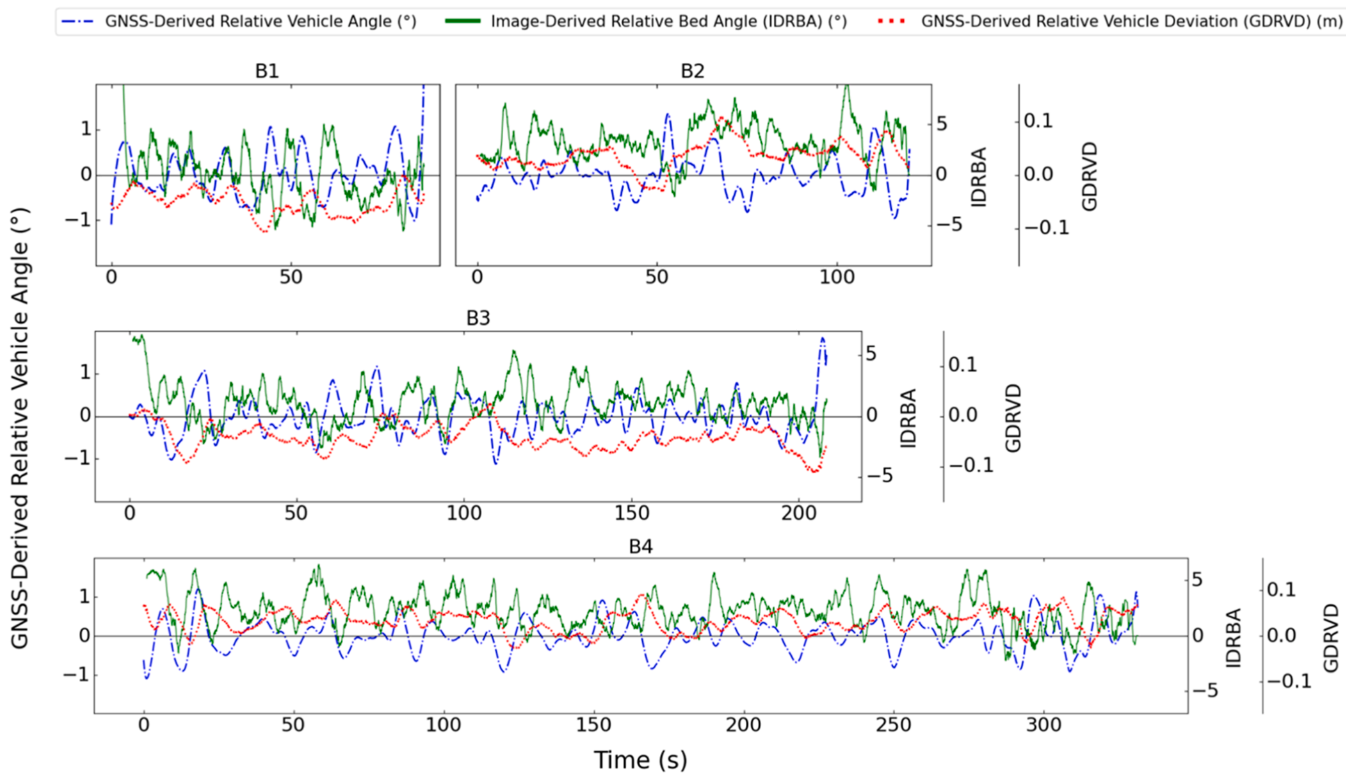

Fig. 9. GNSS-derived relative vehicle angle and deviation vs. image-derived relative bed angle at a ground speed of 1 m/s (B) for beds 1–4.

Table 3
Bed detection failure rates.

Bed ID	Speed (m/s)	Bed detection failure rate (%)	Average across beds
1	0.5	7.24	6.14%
2		13.26	
3		3.35	
4		0.72	
1	1.0	14.79	11.60%
2		16.82	
3		10.31	
4		4.46	

Table 4
Comparison of tracking performance with related studies.

Method	Guidance Sensor	Application	Speed (m/s)	RMSD (m)	MeAD (m)	SD (m)
[15]	RGB binocular	Tractor, cotton	1.2	N/A	0.04	0.05
[7]	NIR binocular	John Deere 7700 tractor, soybean	1.0, 2.0, 3.0	0.03, 0.04, 0.04	N/A	N/A
[11]	LiDAR	High-clearance tractor, vineyard	1.0	0.11	N/A	N/A
Ours	RGB binocular	Skid-steering UGV, loblolly pine	0.5, 1.0	0.05, 0.05	0.05, 0.04	0.02, 0.03

[7]. On the other hand, our guidance system achieved better tracking accuracy compared to a recent LiDAR-based system for vineyards [11]. Meanwhile, it is worth acknowledging that the large vine canopy is less structured than the small pine seedlings, making the detection of the vine row less accurate.

3.5. Limitations and future work

Regarding limitations, the proposed stereo vision-based guidance system was tested at one bareroot forest nursery for seedling size approaching the target size for harvesting. The performance of the proposed guidance system may vary depending on bed condition and seedling size. The bed edge-line detection algorithm relies on a clear, consistent elevation difference between the tractor path and the raised bed and/or between the raised bed and the seedling in the two side rows. If bed edges are not clearly present in the depth image and seedlings are at an early stage, the bed edge-line detection algorithm is likely to fail. However, this can be avoided by re-shaping the beds, which is often done as needed in practice during the growing season. It is expected that once seedlings reach a certain shoot height, the guidance system does not need to depend on the presence of clear bed edges. Future research should test the guidance system for multiple growth stages to identify the threshold for shoot height. The depth image quality of a passive stereo vision camera heavily depends on texture in the stereo image pair. Our study validated the proposed guidance system for an overcast day, however other lighting conditions may affect the guidance performance. Although a sunny day should improve image quality in general, direct sunlight entering the stereo camera at low solar angles could cause poor depth image quality. The camera may be tilted down to mitigate the issue. Additional parameter tuning is likely needed due to the change in bed length in the field of view. The proportional controller operated properly at 0.5 m/s but caused slight understeering at 1 m/s. Tuning a different proportional gain for the higher speed may mitigate the understeering. Future research can consider employing a more advanced method such as model predictive control to achieve optimal performance across different operating speeds. In this study, we used a skid-steering UGV for its low cost and mechanical simplicity. However, skid steering inherently causes greater wheel slippage and soil disturbance than Ackermann steering, which would likely yield more accurate bed-following. Our manual path survey method may be prone to human errors, since the RTK-GNSS receiver's position over bed center was determined visually at each survey point. To improve the survey accuracy in the future, we recommend surveying the target paths using a total station along with an RTK-GNSS unit. An automated alternative would involve using high-precision drone mapping and then extracting bed centerlines from the resulting digital elevation model via image processing techniques. Finally, future work will focus on autonomous, robust traversal of forest nursery beds and headland turning by combining waypoint following and stereo vision-guided bed following.

4. Conclusions

In this study, a stereo vision-based guidance system was developed and tested for a skid-steering UGV to follow raised, curved pine seedling beds in a bareroot forest nursery. We utilized Webots and ROS to develop a depth image processing algorithm for bed edge-line detection and tuned a proportional controller for a UGV model to follow straight simplified nursery beds in simulation. In real-world field tests, the developed guidance system successfully navigated a physical UGV for over 1.4 km of travel along curved seedling beds of four different curvatures at two ground speeds and achieved mean bed-tracking deviations well within acceptable limits without collision and human intervention. The field test results illustrated that the proposed vision system leveraged the difference in elevation between the tractor tracks and the pine seedlings for estimating the UGV heading relative to the bed rather than directly detecting the edges of the raised bed as in the simulation. While the system achieved promising bed following performance in one nursery at a mid-growth stage under an overcast condition, future efforts should enhance the depth image processing and steering control algorithms to robustly handle a variety of bed geometries, soil characteristics, pine seedling heights, lighting conditions, and speeds. In addition, extending the current system to support autonomous headland turning and integrate GNSS-based waypoint navigation would improve the utility and reliability of the proposed method. Overall, this research underscores the potential of low-cost stereo machine vision and depth image processing in automating labor-intensive tasks in bareroot forest nurseries. Integrating such guidance systems with advanced imaging for seedling counting and quality assessment could advance fully automated forest nursery inventory, thereby reducing labor costs and improving nursery management efficiency.

Declaration of generative AI and AI-assisted technologies in the writing process

During the preparation of this work the authors used ChatGPT in order to improve language clarity and readability. After using this tool, the authors reviewed and edited the content as needed and take full responsibility for the content of the publication.

Ethics statement

Not applicable: This manuscript does not include human or animal research.

CRediT authorship contribution statement

Sharif Shabani: Writing – review & editing, Writing – original draft, Visualization, Software, Methodology, Investigation, Data curation. **Ashish R. Mulaka:** Writing – review & editing, Writing – original draft, Visualization, Methodology, Investigation, Formal analysis. **Thomas A. Stokes:** Writing – review & editing, Project administration, Data curation. **Tanzeel U. Rehman:** Writing – review & editing, Resources, Project administration, Funding acquisition. **Yin Bao:** Writing – review & editing, Supervision, Project administration, Methodology, Investigation, Funding acquisition, Conceptualization.

Declaration of competing interest

The authors declare the following financial interests/personal relationships which may be considered as potential competing interests: Yin Bao reports financial support was provided by National Institute of Food and Agriculture. Tanzeel U. Rehman reports financial support was provided by National Institute of Food and Agriculture. Yin Bao reports financial support was provided by Alabama Agricultural Experiment Station. If there are other authors, they declare that they have no known competing financial interests or personal relationships that could have appeared to influence the work reported in this paper.

Acknowledgment

This work is supported by the Agriculture and Food Research Initiative Foundational and Applied Science Program, project awards no. 2022-67021-37860 and 2023-67021-40617, from the U.S. Department of Agriculture's National Institute of Food and Agriculture (USDA NIFA). This work is also supported by the Alabama Agricultural Experiment Station and the Hatch program of the USDA NIFA. The authors would like to thank James Johnson, Bobby Bradford, and Jacob Sizemore for their assistance with fabrication, equipment transportation, and field testing.

Data availability

Data will be made available on request.

References

[1] B. Åstrand, A.J. Baerveldt, A vision based row-following system for agricultural field machinery, Mechatron 15 (2) (2005) 251–269, https://doi.org/10.1016/j.mechatronics.2004.05.005.
[2] R. Bidese-Puhl, Y. Bao, N.D. Payne, T.A. Stokes, R.L. Nadel, S.A. Enebak, In-field pine seedling counting using end-to-end deep learning for inventory management, J. ASABE 66 (2) (2023) 469–477, https://doi.org/10.13031/ja.15383.
[3] G. Bradski, The OpenCV Library, Dr. Dobb's J. Softw. Tools (2000).
[4] R. De Silva, G. Cielniak, J. Gao, Vision based crop row navigation under varying field conditions in arable fields, Comput. Electron. Agric. 217 (2024) 108581, https://doi.org/10.1016/j.compag.2023.108581.
[5] G.M. Domke, S.N. Oswalt, B.F. Walters, R.S. Morin, Tree planting has the potential to increase carbon sequestration capacity of forests in the United States, Proc. Natl. Acad. Sci 117 (40) (2020) 24649–24651, https://doi.org/10.1073/pnas.2010840117.
[6] J. Gai, L. Xiang, L. Tang, Using a depth camera for crop row detection and mapping for under-canopy navigation of agricultural robotic vehicle, Comput. Electron. Agric. 188 (2021) 106301, https://doi.org/10.1016/j.compag.2021.106301.
[7] M. Kise, Q. Zhang, F.R. Más, A stereovision-based crop row detection method for tractor-automated guidance, Biosyst. Eng. 90 (4) (2005) 357–367, https://doi.org/10.1016/j.biosystemseng.2004.12.008.
[8] S. Macenski, T. Foote, B. Gerkey, C. Lalancette, W. Woodall, Robot operating system 2: design, architecture, and uses in the wild, Sci. Rob. 7 (66) (2022) eabm6074, https://doi.org/10.1126/scirobotics.abm6074.
[9] J. Matas, C. Galambos, J. Kittler, Robust detection of lines using the progressive probabilistic Hough transform, Comput. Vis. Image Underst. 78 (1) (2000) 119–137, https://doi.org/10.1006/cviu.1999.0831.
[10] O. Michel, Cyberbotics ltd. webots™: professional mobile robot simulation, Int. J. Adv. Rob. Syst. 1 (1) (2004) 5.
[11] H. Nehme, C. Aubry, T. Solatges, X. Savatier, R. Rossi, R. Boutteau, Lidar-based structure tracking for agricultural robots: application to autonomous navigation in vineyards, J. Intell. Rob. Syst. 103 (4) (2021) 61, https://doi.org/10.1007/s10846-021-01519-7.
[12] C.C. Pike, D.L. Haase, S. Enebak, A. Abrahams, E. Bowersock, L. Mackey, Z. Ma, J. Warren, Forest nursery seedling production in the United States—Fiscal year 2022, Tree Plant. Notes 66 (2) (2023) 20–24.
[13] V.R. Ponnambalam, M. Bakken, R.J. Moore, J. Glenn Omholt Gjevestad, P. Johan From, Autonomous crop row guidance using adaptive multi-roi in strawberry fields, Sens. 20 (18) (2020) 5249, https://doi.org/10.3390/s20185249.
[14] J. Underwood, A. Wendel, B. Schofield, L. McMurray, R. Kimber, Efficient in-field plant phenomics for row-crops with an autonomous ground vehicle, J. Field Rob. 34 (6) (2017) 1061–1083, https://doi.org/10.1002/rob.21728.
[15] S. Zhang, Y. Wang, Z. Zhu, Z. Li, Y. Du, E. Mao, Tractor path tracking control based on binocular vision, Inf. Process. Agric. 5 (4) (2018) 422–432, https://doi.org/10.1016/j.inpa.2018.07.003.